Real-time diffusivity measurements in liquids at several temperatures with one sample

Lyle B. Jalbert, R. Michael Banish, and Franz Rosenberger
Center for Microgravity and Materials Research, University of Alabama in Huntsville, Huntsville, Alabama 35899
(Received 25 September 1997)

Based on the methodology of Codastefano, Di Russo, and Zanza [Rev. Sci. Instrum. **48**, 1650 (1977)], we have developed a technique for the *in situ* measurement of diffusivities in liquids at several temperatures with one sample. In this approach, which circumvents solidification of the diffusion sample prior to concentration profiling, the evolution of the concentration distribution of a radiotracer is followed in real time using two pairs of radiation detectors. A detailed description of the experiment setup and its optimization by computer simulations is given. In experiments with ^{114m}In/In, apparent self-diffusivities were obtained between 300 °C and 900 °C with an uncertainty of ±5%. By utilizing the different self-absorption characteristics of the 24- and 190-keV photons of ^{114m}In, transport in the bulk of the sample and near the container wall was investigated independently. No difference was found. [S1063-651X(98)09002-3]

PACS number(s): 66.10.Cb, 07.85.−m, 07.05.Fb

I. INTRODUCTION

Most techniques to measure diffusion in high-temperature liquids involve solidification of the sample before concentration profiling [1–3]. Inevitable nonuniformities during freezing can introduce considerable concentration redistribution due to segregation [3]. Furthermore, in samples of low thermal conductivity, the heat of solidification can lead to significant temperature nonuniformities. As a result, convective mixing and a higher apparent diffusivity can result even in systems that are perfectly isothermal *during* the liquid diffusion process [3].

Some radial concentration nonuniformities observed in samples that were solidified in diffusion capillaries have been assigned to ''wall effects'' [4]. These effects are perceived, in analogy to surface and grain boundary diffusion, to originate from different diffusion rates near solid walls and in the bulk liquid. However, as pointed out by Nachtrieb [3], the range of true wall effects should be limited to a few atomic dimensions from the wall. This is corroborated by analytical investigations in terms of particle density wave scattering by a wall [5] as well as by molecular-dynamics simulations [6,7]. Both approaches suggest that true wall effects should be limited to some 50 Å from the wall, i.e., to such a small fraction of the sample cross section that they should be undetectable by macroscopic diffusivity measurements.

We have addressed the above problems and developed an experimental technique for real-time measurements of diffusivities in liquids. This radiotracer technique circumvents solidification of the diffusion sample prior to concentration profiling. Furthermore, by employing an isotope that emits photons at (two) sufficiently different energies, transport in the bulk of the sample and near the container wall can be distinguished. In the following, we will present the conceptual considerations underlying this technique, simulations carried out towards its optimization, details of the experimental setup and sample preparation, and applications to self-diffusivity measurements in liquid indium.

II. EXPERIMENT CONCEPT

A. Methodology

The concept underlying our setup was originally developed by Codastefano, Di Russo, and Zanza for diffusivity measurements with gaseous krypton [8]. As schematically indicated in Fig. 1(a), we use an initially solid cylindrical diffusion sample that consists mostly of inactive material (solvent) and a short section of activated isotope, as the diffusant, located at one end. After melting of the sample and heating to a uniform measurement temperature T, the evolution of the diffusant concentration distribution $C(z)$ is monitored through the intensity of the radiation received through

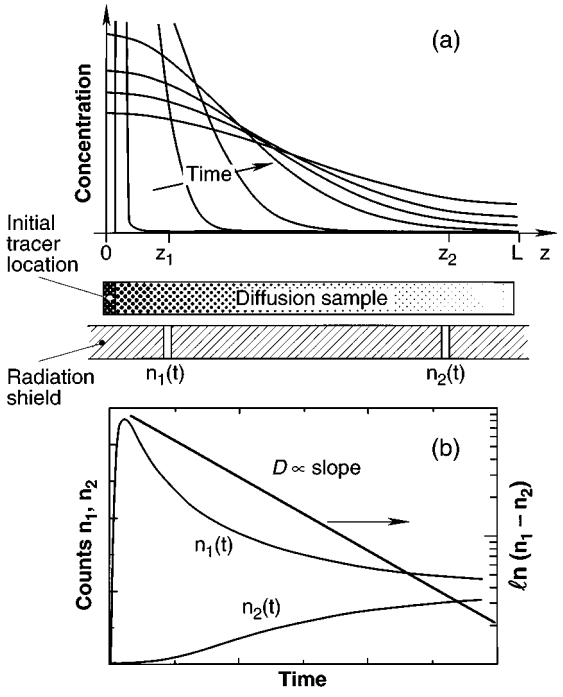

FIG. 1. (a) Schematic presentation of the evolution of the concentration profile and location of the measurement locations. (b) Time traces of the signals at the two measurements locations, and corresponding presentation of the signal difference according to Eq. (2).

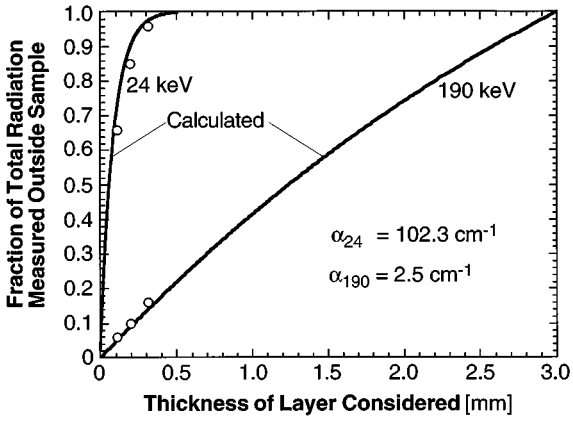

FIG. 2. Emission of 24- and 190-keV photons from 3-mm-thick indium sample containing ^{114m}In versus distance of the emitting atoms from the sample surface.

two bores (collimators) in a radiation shield. These intensities n_1 and n_2 are assumed to be proportional to the concentrations C_1 and C_2, respectively. The characteristic shape of the signal traces $n_1(t)$ and $n_2(t)$ associated with the spreading of the diffusant is plotted in Fig. 1(b).

To satisfy the requirements of the algorithm used to evaluate the diffusivity [8], the radiation collimation bores must be positioned at

$$z_1 = L/6, \quad z_2 = 5L/6, \tag{1}$$

where L is the sample length at the measurement temperature. The diffusivity D is then calculated from the difference of the signal traces using the relation

$$\ln[n_1(t) - n_2(t)] = \text{const} - (\pi/L)^2 Dt, \tag{2}$$

where the constant depends on the concentration profile $C_0(z)$ at the beginning of the measurement. Since the $C_0(z)$ does not explicitly enter the D evaluation, diffusivities can be consecutively determined at several temperatures during the spreading of the concentration profile in the same sample. Obviously, before the first measurement, $C_0(z)$ must have spread enough to provide a significant signal at both detector locations.

In addition to its real-time feature, an isotopic labeling technique permits investigations of the perceived ''wall effect'' mentioned in the Introduction. By employing an isotope that emits photons at two sufficiently different energies and thus different self-absorption behavior, transport in the bulk of the sample and near the container wall can be distinguished to some extent. Figure 2 illustrates this approach. Based on the attenuation data for 24- and 190-keV photons of ^{114m}In [9], we have calculated the fraction of the total radiation received at the two different emission energies outside a 3-mm-thick sample vs the distance of the emitter from the surface of the sample; for details of the one-dimensional slab model used see Refs. [10,11]. Note that the 24-keV photons received are predicted to originate in essence only from a 300-μm-deep surface layer. The 190-keV photons, on the other hand, stem from throughout the whole sample slab. Thus, using an appropriate detector circuit with energy discrimination capability (see Sec. IV C), transport near the wall of the sample container and in the sample bulk can be distinguished to some extent.

We have experimentally confirmed the above selective absorption behavior. Indium disks of 100, 200, and 300 μm thickness were prepared from indium that had been uniformly diffusion doped with ^{114m}In. The normalized ratios of the 24- and 190-keV counts received from these disks agreed well with the predicted values; see the data points on the curves in Fig. 2.

B. Collimator positions and thermal expansion

Relation (2) is based on the specific location requirement for the detectors given by Eq. (1) with respect to the sample length L. For applications of this measurement technique at several temperatures with one sample, corrections are required to account for thermally induced changes in sample dimension and collimator locations. For these corrections it is advantageous to use two pairs of collimation bores and detectors. They are positioned such that, taking into account the thermal expansion of the sample, support structure, and radiation shield, one pair fulfills condition (1) at the lowest measurement temperature and the other pair at the highest. As a consequence, for all intermediate temperatures, there is always a collimation bore above and below the exact positions required. (Note that the size and fixed position of the detectors is chosen such that most of the radiation emanating from a ''moving'' collimator remains detected; see also Sec. IV B).

For the corrections we assume that A and B, respectively, are the diffusant concentrations at the collimator positions z^- and z^+ that bracket the concentration C at the accurate measurement position z_m defined by Eq. (1). Then, noting that, at the stage where sufficient signal is obtained at the second collimators, the curvature of the concentration profile is small, we approximate the C at z_m by the linear interpolation

$$C = \left(\frac{z^+ - z_m}{z^+ - z^-}\right) A + \left(\frac{z_m - z^-}{z^+ - z^-}\right) B. \tag{3}$$

III. EXPERIMENT SIMULATION AND OPTIMIZATION

We have carried out detailed computer simulations to optimize the experiment setup with respect to sample size and activity, measurement accuracy, and number of $D(T)$ data obtainable with one sample. In the following we derive the basic relations used; for more details on the simulations the reader is referred to Ref. [10].

A. Evolution of concentration distributions including sample expansion

In a realistic simulation of the experiments, changes in sample length due to thermal expansion during heating to the first measurement temperature and heating or cooling to consecutive temperatures must be taken into account. Let the initial concentration profile in the sample of total length L_1 at temperature T_1 be

$$g(z) = C_0 \theta(z - l_i), \quad 0 < z < L_1, \tag{4}$$

with C_0 the initial concentration over the initial length of the activated section l_i and $\theta(z - l_i)$ a step function equal to 1 for $z < l_i$ and 0 for $z > l_i$. With this initial condition and the closed-system boundary condition

$$C_z(0,t)=C_z(L_1,t)=0, \quad 0<t, \tag{5}$$

assuming that the diffusivity D is independent of concentration and coordinate z, one obtains from Fick's second law

$$C_t(z,t)=DC_{zz}(z,t) \tag{6}$$

a general solution for the evolving concentration distribution in the form [12]

$$C(z,t)=a_0+\sum_{n=1}^{\infty} a_n \cos\left(\frac{n\pi z}{L_1}\right)\exp\left[-\left(\frac{n\pi}{L_1}\right)^2 Dt\right], \tag{7}$$

with the Fourier coefficients

$$a_0=\frac{1}{L_1}\int_0^{L_1} g(z)dz \tag{8}$$

and

$$a_n=\frac{2}{L_1}\int_0^{L_1} g(z)\cos\left(\frac{n\pi z}{L_1}\right)dz. \tag{9}$$

Thus, after time t_1 at T_1 with diffusivity D_1,

$$C_1(z,t_1)=\frac{C_0 l_i}{L_1}+\sum_{n=1}^{\infty}\frac{2C_0}{n\pi}\sin\left(\frac{n\pi l_i}{L_1}\right)\cos\left(\frac{n\pi z}{L_1}\right)\times\exp\left[-\left(\frac{n\pi}{L_1}\right)^2 D_1 t_1\right]. \tag{10}$$

Next we assume that during the transition from T_1 to a T_2, the diffusive redistribution is insignificant. In view of he high ratio of thermal to solutal diffusivity of the materials under consideration, this is readily achievable in practice with rapid temperature ramping. Furthermore, we ignore the diffusant redistribution *due to* the thermal expansion or contraction of the sample during the temperature change. With typical thermal expansion coefficients of liquids, this simplification introduces significant errors only for simulation temperature changes in excess of 200 °C. Based on these assumptions, the initial condition at T_2 is taken as

$$g_2(z)=C_1(z,t_1). \tag{11}$$

Thus, accounting for the new sample length L_2, Eqs. (7)–(9) yield for the evolution of the concentration distribution at T_2 [10]

$$C_2(z,t)=a_{02}+\sum_{m=1}^{\infty} a_{m2}\cos\left(\frac{m\pi z}{L_2}\right)\exp\left[-\left(\frac{m\pi}{L_2}\right)^2 D_2 t\right], \tag{12}$$

where

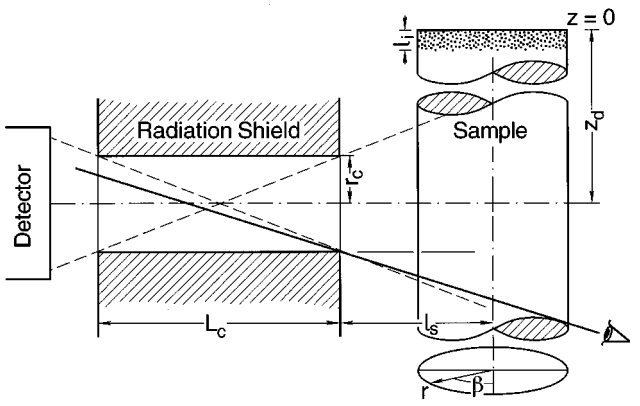

FIG. 3. Definition of sample-collimator-detector geometry for the view factor calculation.

$$a_{02}=\frac{C_0 l_i}{L_1}+\sum_{n=1}^{\infty}\frac{A_n}{L_2}\frac{L_1}{n\pi}\sin\left(\frac{n\pi L_2}{L_1}\right), \tag{13}$$

with

$$A_n=\frac{2C_0}{n\pi}\sin\left(\frac{n\pi l_i}{L_1}\right)\exp\left[-\left(\frac{n\pi}{L_1}\right)^2 D_1 t_1\right] \tag{14}$$

and

$$a_{m2}=\frac{2C_0 l_i}{m\pi L_1}\sin(m\pi)+\sum_{n=1}^{\infty}\frac{A_n}{\pi L_2}\left[\frac{\sin\left[\left(\frac{n}{L_1}-\frac{m}{L_2}\right)\pi L_2\right]}{\frac{n}{L_1}-\frac{m}{L_2}}+\frac{\sin\left[\left(\frac{n}{L_1}+\frac{m}{L_2}\right)\pi L_2\right]}{\frac{n}{L_1}+\frac{m}{L_2}}\right]. \tag{15}$$

Based on this formulation, we have simulated the evolution of the concentration distribution during entire experiment scenarios, including the multistep ramps to the first and consecutive measurement tempeatures [10].

B. View factor, absorption of radiation, and detector noise

For realistic estimates of the radiation received at the detector, the volume of sample visible through the collimation hole must be known. Hence we have calculated the view factor of the sample-collimator-detector geometry [10]. Assuming perfect absorption by the shield material, radiation escapes only through the collimation bore of diameter $2r_c$ and length L_c; see Fig. 3. Under this assumption, the number of emitters ''seen'' by the detector is

$$N(z_d)=\int_{-\pi/2}^{\pi/2}\int_0^{r_c}\int_{z_d-z_0}^{z_d+z_0}\frac{r_c^2\left\{2\cos^{-1}\left(\frac{h}{r_c}\right)-\sin\left[2\cos^{-1}\left(\frac{h}{r_c}\right)\right]\right\}rC(z)}{2\pi r_t^2}\,dz\,dr\,d\beta, \tag{16}$$

where

$$h=\frac{L_c}{2(l_s+r\ \sin\ \beta)}\ (\sqrt{r^2\ \cos^2\ \beta+z_0^2}-r_c)$$
$$\times\theta(\sqrt{r^2\ \cos^2\ \beta+z_0^2}-r_c), \quad (17)$$

$$z_0=\sqrt{\left(\frac{r_c}{L_c}\left[L_c+2(l_s+r\ \sin\ \beta)\right]\right)^2-r^2\ \cos^2\ \beta}, \quad (18)$$

$r_t=(L_c+l_s)$ and $C(z)$ at the time of measurement is given by an equation similar to Eq. (12). As defined in Fig. 3, r,β,z are the coordinates within the sample, with $z=0$ at the end containing the radiation source of initial thickness l_i. The angle $\beta=-\pi/2$ is taken in the direction of the detector on the collimator axis.

In the actual simulation runs, we have included the attenuation of the radiation by both the emitter-location-dependent self-absorption (see Fig. 2) and the thermal radiation shields (see Fig. 6). Furthermore, the noise in the detectors, i.e., the uncertainty in the detector signals due to radiation counting statistics, was accounted for. This noise is of the order of $\sqrt{n}$, where n is the number of counts received. Thus the statistical uncertainty increases with counts, but the relative uncertainty decreases as $1/\sqrt{n}$ [9]. Hence the higher the count rate, the more accurate the results. This can be accomplished by either using a long counting period or high initial activity.

C. Sample dimensions and activity

The lengths of the activated section l_i and the overall sample L were optimized based on the following considerations. The above square-root dependence of the detector noise on sample activity suggests the use of high activities to maximize the resolution in the difference of the two detector signals. This in turn minimizes the measurement time required at a given temperature and thus the errors from continuous diffusion during a data acquisition period. Similarly, the initial activity required to ensure a given detector signal increases with sample length. However, low activity levels are desirable for radiation safety reasons. Simulation results (see Sec. III E) showed that an initial activity of 5 mCi provides sufficient resolution. With this initial activity, the optimum sample length is 30 mm [10].

To determine the length of the activated section l_i we recall our assumption that the part of the concentration profile viewed by a detector is linear; see Eq. (3). Thus the initially activated section must be short enough that the transient in which the spreading concentration distribution possesses significant curvature is over when the signal level at the second detector is high enough to begin measurements. The simulations yielded $l_i=1$ mm as optimum. Thus our diffusion samples consist initially of two parts: the 1-mm-long radioactive section and a 29-mm-long non-activated section.

D. Determination of collimator geometry

Geometric factors as well as radiation properties of the shielding material must be considered in optimizing the collimator geometry. Obviously, the radiation shield must be thick enough to absorb a large fraction of the radiation. Otherwise the detector signal is not representative of the radiation escaping through the collimation bores. Furthermore, as can be seen from Fig. 3, due to the conical shape of the radiation beam transmitted by the collimation bore, r_c's larger than the sample diameter will not result in a commensurate increase of the radiation dose received by the detector. These arguments are further complicated by the scattering of and fluorescence induced by the primary radiation [9]. Our samples (^{114m}In) emit about 95% γ and 5% β radiation, with the average β energy in excess of 750 keV. Both cause fluorescence in the shield. In addition, γ radiation is Compton scattered in the shield and, in particular, upon grazing incidence on the collimator surface. Each scattering process reduces the energy of the radiation. Thus multiple scattering and fluorescence can lead to photons that are counted in energy windows different from those corresponding to the primary photons and β particles.

We have experimentally investigated various collimator geometries for their effect on total radiation received by the detector. Hence we used lead for the collimator optimization experiments that were conducted at room temperature. Collimation holes of 1, 1.5, 2, and 3 mm diameter were drilled into lead shields of 12.7, 25.5, and 38.3 mm thickness. A 3-mm-diam cylindrical radioactive indium sample was placed consecutively behind the collimation bores. The detector signals were energy discriminated; see Sec. IV C. Table I summarizes the results. The signal-to-noise ratio is defined as the signal amplitude obtained in the energy window (± 0.3 keV about the chosen energy) divided by the sum of amplitudes measured in all other channels outside the energy window.

From these data, we can draw the following conclusions. Since the signal-to-noise ratio (SNR) for the 1-mm collimator hole is essentially 1, the smallest usable diameter is 1.5 mm. As expected, with the 3-mm sample diameter very little additional radiation is received on expanding the collimator diameter to more than 2 mm and, hence, the SNR remains essentially unchanged or even decreases. Furthermore, the signal-to-noise ratio increases with the increase in the thickness of the radiation shield, from 12.7 mm to 25.5 mm, while a 38.3 mm thickness results in little further improvement.

Copper, initially planned as the high-temperature radiation shield material, showed intolerably high fluorescence levels. For the actual high-temperature experiments, the radiation shield consisted of gold with a wall thickness of 15.5 mm. As calculated from absorption data [9], this wall thickness provides the same absorption for 190-keV photons as the 25.5 mm of lead used above. This results in an overall diameter of the radiation shield/isothermal liner of 41 mm. With this collimator geometry and 10-mm square detectors, the maximum distance between the outside edge of the collimator and detector must not exceed 30 mm if all radiation from the collimators is to be collected.

E. Simulated multitemperature experiments

Based on the above considerations, utilizing Eqs. (1)–(18) evaluated for the optimized dimensions of our experimental hardware, simulations were carried out to explore the feasibility and accuracy of measurements at several temperatures with the same sample. Table II shows for self-diffusion in indium that a temperature range of 700 °C can be covered in

TABLE I. Signal-to-noise ratios obtained with various collimator geometries.

Diameter (mm)	Lead thickness (mm)	Signal to noise ratio at 24 keV	Signal to noise ratio at 190 keV
1	12.7	1.1	1.1
1.5	12.7	1.4	1.25
2	12.7	1.67	1.5
3	12.7	2.1	2.0
1	25.5	1	1
1.5	25.5	1.6	1.6
2	25.5	2.0	1.8
3	25.5	2.0	2.1
1	38.3	1	1
1.5	38.3	1.9	1.5
2	38.3	2.2	1.9
3	38.3	1.7	2.2

100 °C increments using only two samples. The second column lists the input diffusivities [13] used in the simulations. The table illustrates well the importance of taking the detector noise into account. Without superposition of noise on the signals $n_1(t)$ and $n_2(t)$, the simulations unrealistically yield an error in all eight deduced diffusivity values of less than 0.2%; see the third and fourth columns. However, as shown by columns six and seven, on superposition of a realistic $\pm(O)2\sqrt{n}$ noise level, the errors increase to (a still very acceptable) 1.5%.

Note that it is advantageous to begin with the highest temperature and, thus, highest diffusivity in a measurement series and then to take data at consecutively lower temperatures. Obviously, at the highest diffusivity the time required until the signal at the second detector rises above background is minimized; see Eqs. (7)–(9). In addition, the simulations unexpectedly revealed another advantage of decreasing temperature sequences, in which the measurement time at each temperature is shorter than at the immediately following one. While at all temperatures the spreading of the concentration profile depends on the product of the respective D and measurement time [see Eqs. (7) and (12)], beginning with the second temperature there is an additional time-dependent spreading term [see Eq. (14)]. As a consequence, longer measurement times at the prior temperature, as they would be required in a sequence with increasing temperatures, cause a larger decrease in the overall concentration gradient. The simulations show that the resulting smaller differences between the two signals lead to fewer feasible temperatures in an experiment.

The above simulations provided valuable guidance for experiment design. However, they do not account for some of the error sources present in actual experiments. These include imperfect shielding and secondary scatter by the radiation shield and collimation bores. In Sec. IV D we will present procedures to at least partly correct for these errors using signals from background detectors. There are also significant systematic errors associated with the dimensional tolerances of the sample and collimator-detector geometry. These error sources are evaluated in Sec. IV E.

IV. EXPERIMENT

A. Sample preparation and containment

The sample consists of two parts: a short radioactive section and a long nonactivated section. The preparation and containment of these sections is based on the following considerations. Uncertainties in the sample geometry are the major error source in these experiments. Furthermore, the sample cross section must be uniform to assure one-

TABLE II. Comparison of simulation model input diffusivities and simulation results for two model runs at eight different temperatures.

Temperature (°C)	Input	Result without noise		Result with noise	
	10^5D (cm^2/sec)	10^5D (cm^2/sec)	% error	10^5D (cm^2/sec)	% error range
900	10.2226	10.2002	0.22	10.2589	<0.5
700	8.260 01	8.255 02	0.060	8.185 63	<1
500	5.978 81	5.978 31	0.0084	5.956 64	<1
300	3.456 23	3.456 21	0.000 72	3.498 95	<1.5
800	9.280 63	9.25 65	0.26	9.331 37	<0.5
600	7.158 44	7.154 24	0.059	7.100 53	<1
400	4.734 12	4.733 54	0.012	4.723 77	<1
200	2.210 22	2.2102	0.000 83	2.210 52	<1.5

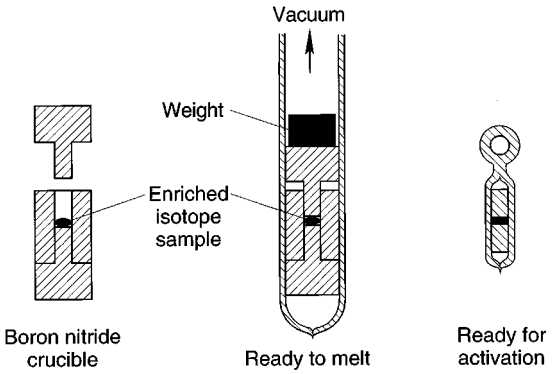

FIG. 4. Steps for preparation of the enriched isotope pellet for activation.

dimensional diffusion. Nonuniformities in the cross section can arise from capillarity (rounded edges at ends of both sections) and voids or bubbles in the sample bulk and at the interface between the two sample sections. Equally important is the accuracy in sample length and volume; see Sec. IV E. In addition, oxidation, in particular of the contacting ends of the sections, can form a diffusion-resistant layer. Hence, both the indium and boron nitride (BN) (Carborundum grade AXO5) container parts (BN is not wet by indium) are thoroughly high-vacuum baked (10^{-6} mm of Hg at 900 °C) to remove gaseous contaminants.

The radioactive section is prepared, as shown in Fig. 4, using a boron nitride crucible consisting of three parts machined with tight tolerances. After insertion of the bottom plug into the 3-mm-i.d. cylinder, a bead of indium (40% enriched in ^{113}In) is put in place. The weight of the bead is chosen such that the thickness of the final disk will be approximately 1 mm. After insertion of the top plug, the whole crucible, with a small weight on the top, is inserted into a glass tube. This is followed by vacuum heating to 900 °C and solidification of the sample under high vacuum while it is compressed by the weight. After cooling, we backfill with argon. Then the section is prepared for irradiation. Utilizing a glove box, the glass tube is broken and the sample is transferred to a 3-mm-diam glass capillary. To facilitate sample removal after irradiation, 5-mm-long rods are placed above and below the sample prior to sealing of the capillary. The sealed-in section is then sent to the reactor for activation by fast neutron irradiation.

The 29-mm-long nonactivated section of the sample is cast in place under high vacuum at 900 °C in the boron nitride ampoule used for the diffusion measurements. As depicted in Fig. 5, this 7-mm-o.d. ampoule is 60 mm long and has a 3-mm precision-reamed bore. To ensure the proper sample length we require square corners on the top and bottom ends of the sample. At the bottom this is achieved by press fitting a BN plug into the ampoule bore. At the top we apply a slight pressure on the sample with a weak graphite spring [Energy Science Laboratories, force 29.4 mN (3 g) at 900 °C] against a BN plunger that has less than 0.025-mm clearance in the bore. To establish conditions that ensure the absence of void formation, inactive sections were repeatedly melted, solidified, and x-ray inspected.

Then the activated section is transferred into the ampoule in a glove box flushed with an inert gas. After replacing the plunger and spring, the BN ampoule is mechanically closed with the BN screw lid and inserted into the square-bottom silica tube, which, in turn, is evacuated and sealed.

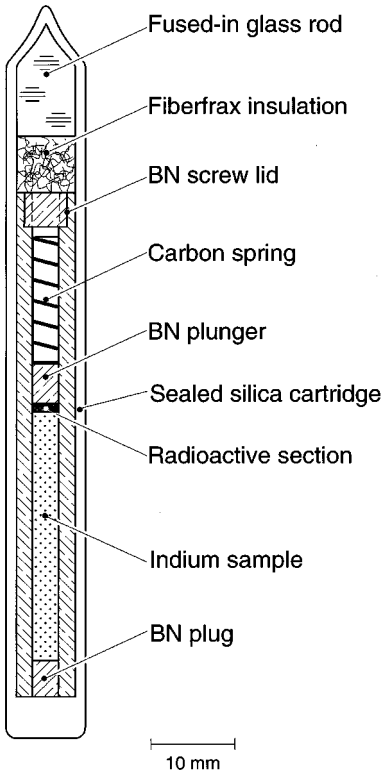

FIG. 5. Cross section of diffusion sample cartridge.

B. Diffusion measurement apparatus

The apparatus, which accommodates the above sealed diffusion sample cartridge, consists of the following components (see also Fig. 6). There is a gold radiation shield and isothermal liner (90 mm long, 41 mm in diameter). Gold was chosen because of its high melting point and thermal conductivity together with the low fluorescence and high radiation absorption properties. To minimize displacement of this gold cell by thermal expansion it is supported by a silica pedestal (thermal expansion coefficient 5.5×10^{-7} cm/cm °C). There is a stainless-steel-encased, ceramically insulated resistance heater (Fast Heat, 130 mm long, 120 V, 5 A). To avoid radiation absorption, the heater has six holes (7 mm in diameter) at the positions of the collimators and background detectors. Thermocouples (type *K*) are inserted into the gold liner for temperature uniformity control. One of these provides input to a temperature controller and silicon controlled rectifier that stabilizes the temperature to better than ±0.5 °C. An inner thermal radiation shield consists of a stainless-steel sheet. An outer thermal shield consists of gold-coated boro-silicate glass. There are six radiation detectors (not shown): one pair each aligned with the oppositely placed, differently spaced radiation bores (see Sec. II B) and one pair 90° off the measurement-detector plane to record the background radiation. Top and base plates contain the measurement structure. Axial heat losses from the heated components to these plates are minimized by Fiberfrax insulation.

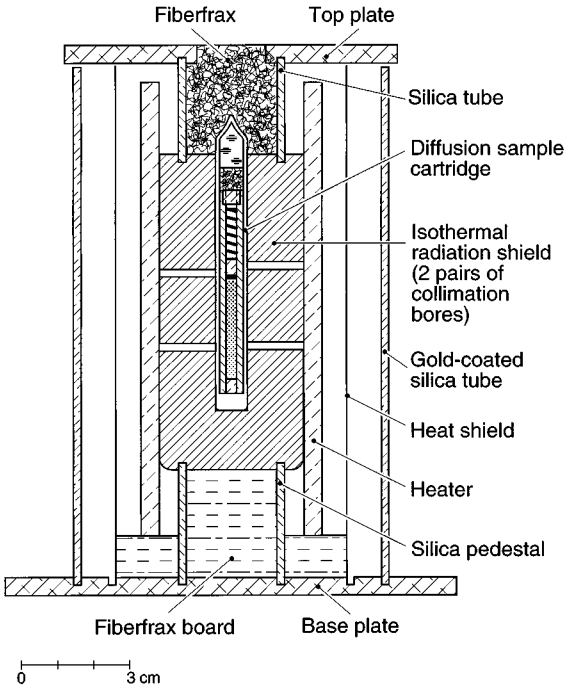

FIG. 6. Cross section of diffusion measurement apparatus (without detectors and electronics). Note the two pairs of collimation bores, offset with respect to each other, to cover the temperature range 300 °C–900 °C for indium.

The temperature uniformity across the diffusion sample in this apparatus was checked using a dummy diffusion sample cartridge with eight built-in, calibrated thermocouples (type *K*, sheath diameter 0.5 mm, Omega Engrg.). At 500 °C, the vertical temperature difference ΔT_v across the indium sample (see Fig. 5) was 0.4 °C, with the bottom cooler than the top. At the same time the maximum horizontal ΔT_h, which occurred at about midheight of the sample, was 0.3 °C. At 900 °C, we obtained a $\Delta T_v = 1.4$ °C of the same orientation and a maximum $\Delta T_h = 0.4$ °C at the top of the sample.

An important design consideration for the use of the apparatus over a wide temperature range is the thermal expansion of the components, which changes the spacing of the collimation bores and their position with respect to the detectors. The changes in the bore spacing, which over a temperature range of 700 °C is about 0.4 mm, is taken into account when applying Eq. (3). The changing bore locations with respect to the fixed detector positions are taken into account by using detector crystals large enough that the emanating radiation cone remains fully detected during the thermal displacement.

C. Detectors, discriminators, and calibration

After examining numerous detector types, we have found that $Cd_xZn_{1-x}Te$ crystals (eV Products, 1 cm^2 and 3 mm thick) provide a quantum efficiency of approximately 1 for the 24-keV photons and 0.35 for the 190-keV photons of indium. In addition, these detectors exhibit a low noise threshold ($\leqslant$10 keV) at temperatures $\leqslant$50 °C, i.e., no additional cooling is required. Two single-channel analyzers (SCAs) per detector can be set using four potentiometers on the circuit boards providing a 0–250 keV energy range.

Due to differences in the characteristics of individual crystals and detector circuits each detector must be independently calibrated. The calibration is accomplished using a multiple-channel analyzer (MCA) (Accuspec, NaI, Canberra Instruments) and a data acquisition system with a counter for each energy channel. The calibration of each detector SCA energy window is performed by matching the SCA output count rate and the chosen MCA energy window count rate.

D. Measurement procedure

After loading the sealed sample ampoule into the gold cell and repacking the thermal insulation, the temperature is ramped at 15 °C/min to the highest experiment temperature. After the signal at the $5L/6$ detectors has sufficiently risen above background, data acquisition begins. The measurement times at this first and consecutive, lower temperatures are predetermined based on the simulation results. After diffusant uniformity has been obtained throughout the sample, we return to each experiment temperature and collect baseline averages. These data are used to correct for inconsistencies of the detector crystals and possible abnormalities in the collimator-detector geometry. One detector-channel is selected as being ''correct'' and, using the averages at each temperature, all other channels are proportionally adjusted. The same is done with the two background detectors. The background is subtracted from all channels and then Eq. (3) is applied to find the concentration at all times.

With sources activated to 5–10 mCi we can typically obtain data at three separate temperatures per run. The simulations suggested the feasibility of four temperatures. However, in the simulation we did not allow for cool down periods between temperatures. At lower temperatures these periods can be up to an hour for a 200 °C change.

E. Estimation of uncertainty in apparent diffusivity

As expressed in Eq. (2), the diffusivity D is obtained from the slope of a straight line fit to $\ln[n_1(t)-n_2(t)]$. We have shown earlier that such straight line plots can be obtained even in diffusion experiments with considerable convective contamination [14]. Hence, considering the deviations from isothermality of our samples (see Sec. IV B) and thus likely resulting convective transport, the following estimate of uncertainty in D must be understood with respect to the apparent rather than the true diffusivity. This uncertainty can be expressed in terms of the uncertainties in the slope and the sample length as [15]

$$\delta D = \sqrt{\left[\left(\frac{L}{\pi}\right)^2 \sigma_B\right]^2 + \left(\frac{2LB}{2}\,\delta L\right)^2}, \tag{19}$$

where the slope $B = -\pi^2 D/L^2$ and $\sigma_B^2 = N\sigma_y^2/\Delta$, with N the number of data points used in the fit, and $\Delta = N(\Sigma_{i=1}^N t_i^2) - (\Sigma_{i=1}^N t_i)^2$ and $\sigma_y^2 = [1/(N-2)]\Sigma_{i=1}^N (y_i - A - Bt_i)^2$, with $y = \ln(n_2 - n_1)$ and A (the y intercept)=const.

The uncertainty in the length of the sample can be estimated as follows. The sample is made of two sections (see Sec. III C) producing an uncertainty

TABLE III. Apparent self-diffusivities obtained with indium at the two photon energies in four experiments.

Temperature (°C)	190 keV ($10^5 D$ cm^2/sec)	24 keV ($10^5 D$ cm^2/sec)
800	9.84±0.59	10.07±0.61
600	7.69±0.48	8.02±0.50
400	5.25±0.34	5.01±0.34
700	7.72±0.47	
500	6.20±0.39	
300	4.60±0.33	
900	8.95±0.54	8.61±0.52
800	9.80±0.59	10.16±0.61
700	8.93±0.55	9.62±0.60
900	11.75±0.70	11.63±0.59
600	8.04±0.49	8.09±0.50
300	4.54±0.29	4.78±0.31

$$\delta L = \delta l_i + \delta l_{\mathrm{NA}}, \tag{20}$$

where l_{NA} is the length of nonactivated sample. The uncertainty in the two sections is determined from the volume and machining of the crucibles such that

$$\delta l = \sqrt{\left(\frac{1}{\pi r^2}\,\delta V\right)^2 + \left(\frac{2V}{\pi r^3}\,\delta r\right)^2}, \tag{21}$$

with r the radius of the crucible and V the volume of sample material. If we assume that the density ρ is accurately known, then the uncertainty in the volume is

$$\delta V = \left|\frac{1}{\rho}\right| \delta m. \tag{22}$$

The tolerance on the crucibles is ±0.0127 mm (nominal sample inner diameter 3.01 mm). Due to the repeated vacuum melting, the uncertainty in the masses is 0.001 g.

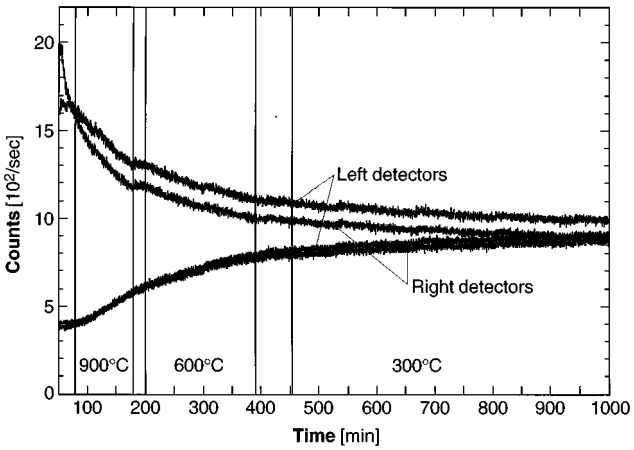

FIG. 7. Original signal traces for 190-keV photons during the 900 °C–300 °C run.

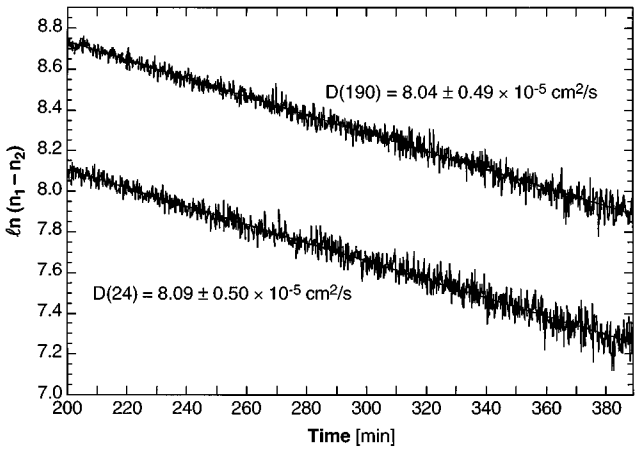

FIG. 8. Plot of 600 °C data of 900 °C–300 °C according to Eq. (2), together with diffusivities obtained from least-squares fits (straight lines).

Substituting Eq. (22) into Eq. (21) and the result into Eq. (20), the uncertainty in the length of the sample is ±1.02 mm for indium.

The σ_B error is directly related to the counting statistics. This error is minimized with high initial activities. With the activity levels chosen for these experiments we find that the second term in Eq. (19) is up to an order of magnitude larger than the first.

V. RESULTS AND DISCUSSION

Several diffusion runs with indium were carried out. Each run covered three consecutively lower temperatures. The results are summarized in Table III. The error estimates are based on Eq. (19). The lack of 24-keV data for the one run is due to failure of one low-energy channel. Note that, within the uncertainty of the data, no difference between transport (diffusion) in the bulk and near the wall is apparent.

As-measured time traces of the 190-keV signals obtained in the 900 °C–300 °C run (Table III) are shown in Fig. 7. These plots reveal several features of the method. The right top detector has the highest initial count rate since its position $z_1 = L/6$ has been chosen for the highest $T = 900$ °C, i.e., the longest L; see Sec. II B. The change in the diffusion coefficient at the three temperatures is visible in the slope changes of the data. Furthermore, the contraction of the sample on temperature decrease is evident from the rise in the count rate. One sees also that the final count rates of the detectors differ, due to the individual characteristics of the detector crystals; see Sec. IV D. A plot of $\ln(n_1 - n_2)$ vs time, resulting from similar curves obtained at 600 °C after their base-line corrections, is shown in Fig. 8 together with the least-squares fits for both energies.

All data from Table III together with the self-diffusivities of In measured by other authors [4,13,16,17,18], are plotted in Fig. 9. The wide scatter of the data illustrates well that diffusivities obtained in liquids at normal gravity are prone to be contaminated by uncontrollable convection. As emphasized for liquid diffusivity measurements by Verhoeven [19], any horizontal component of a density gradient results in convection without a threshold. We have recently estimated

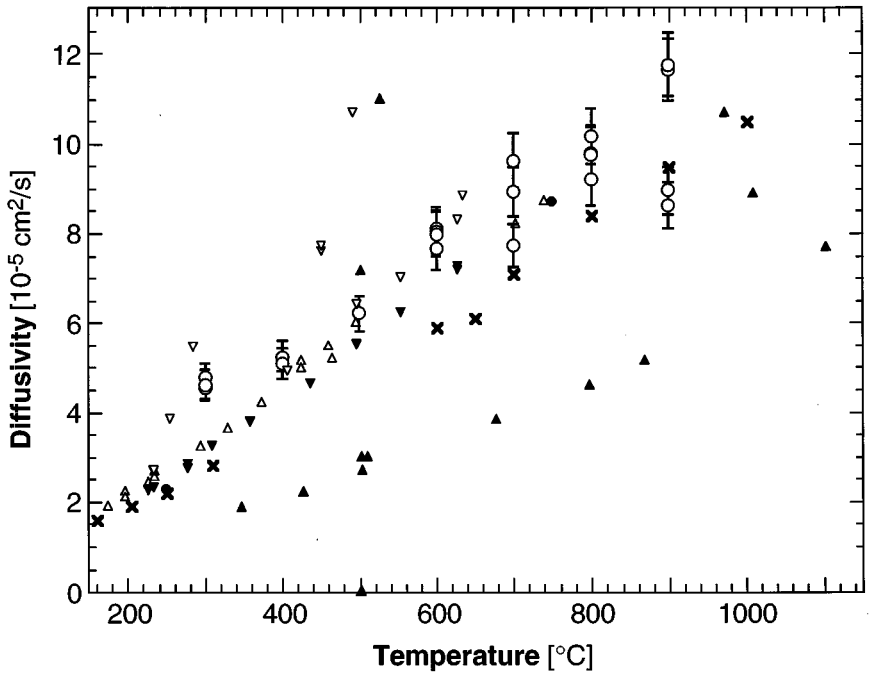

FIG. 9. Experimental data for self-diffusivities in indium: ○ this work; ▲ Foster and Reynik [17]; △ Lodding [13]; ● Mathiak *et al.* [16]; ▽ and ▼ Carreri, Paoletti, and Vincentini [4] with 1.6- and 0.83-mm-diam capillaries, respectively. Ogloblya, Lozovoi, and Chumakov [18] with 0.5-mm-diam capillaries.

convective contributions to transport in our experiments [14]. The numerical modeling results for self-diffusion in In at 730 °C in 30-mm-long capillaries, 3 mm in diameter, show that at normal gravity convective contributions become significant when an applied horizontal temperature non-uniformity ΔT_h exceeds 0.01 K. Often, flow due to horizontal density gradients can be reduced by keeping, as is the case in our experiments (see Sec. IV B) the top of the sample slightly warmer than its bottom. However, the above simulations [14] show that this can be rather ineffective and under certain conditions may even increase the apparent diffusivity.

From the above, it is not surprising that our data show evidence of convection in the samples. For instance, the apparent D at 700 °C deduced from the 900 °C–700 °C run is significantly higher than that of the 700 °C–300 °C run. This may be due to the longer time the first sample was at high temperature before the measurement at 700 °C was made. Thus there was more time for convective contamination of the diffusive transport. Note, however, that the uncertainties for the two measurements at 900 °C do not overlap. We assign this to possible inconsistencies in the sample preparation and convective contributions. The low value may be the result of partial blockage of the diffusion path by either a void or an oxidation layer between the active and inactive sections of the sample.

IV. SUMMARY AND CONCLUSIONS

We have developed and systematically optimized a technique for the *in situ* measurement of diffusivities in liquids at several temperatures with one sample. This approach circumvents the solidification of the diffusion sample required by other methods, which can result in significant errors. In experiments with ^{114m}In/In, apparent self-diffusivities were obtained between 300 °C and 900 °C with an uncertainty of ±5%. By utilizing the different self-absorption characteristics of the 24- and 190-keV photons of ^{114m}In, transport in the bulk of the sample and near the container wall was investigated independently. No differences were found. There is clear evidence for convective contamination of our data. To obtain increased accuracy in the diffusivity values, we plan to perform these experiments in a low-gravity environment.

ACKNOWLEDGMENTS

We thank W. F. Kaukler from our center for help with the x-ray inspection of diffusion samples. L. Carver has expertly prepared the figures. Support for this work by the Microgravity Science and Applications Division of the National Aeronautics and Space Administration through Contract No. NAS8-39716 is gratefully acknowledged.

[1] M. Shimoji and T. Itami, *Atomic Transport in Liquid Metals* (Trans Tech, Aedermansdorf, 1986).

[2] N. H. Nachtrieb, Ber. Bunsenges. **80**, 678 (1976).

[3] N. H. Nachtrieb, in *Proceedings of the International Conference on Properties in Liquid Metals*, edited by P. D. Adams, H. A. Davies, and S. G. Epstein (Taylor and Francis, London, 1967), p. 309.

[4] G. Careri, A. Paoletti, and M. Vincentini, Nuovo Cimento **10**, 1088 (1958).

[5] M. Fixman, J. Chem. Phys. **29**, 540 (1958).

[6] S. B. Savage and R. Dai, Mech. Mater. **16**, 225 (1993).
[7] G. Mo and F. Rosenberger, Phys. Rev. A **44**, 4978 (1991).
[8] P. Codastefano, A. Di Russo, and V. Zanza, Rev. Sci. Instrum. **48**, 1650 (1977).
[9] W. H. Tait, *Radiation Detection* (Butterworths, London 1980).
[10] L. Jalbert, Ph.D. dissertation, University of Alabama, Huntsville, 1997 (unpublished).
[11] N. Tsoulfanidis, *Measurement and Detection of Radiation* (McGraw-Hill, Washington, DC, 1983).
[12] J. Crank, *The Mathematics of Diffusion* (Clarendon, Oxford, 1956).
[13] V. A. Lodding, Z. Naturforsch. **11A**, 200 (1956).
[14] I. Alexander, J.-F. Ramus, and F. Rosenberger, Microgravity Sci. Technol. **9**, 158 (1996).
[15] J. R. Taylor, *An Introduction to Error Analysis* (University Science Books, Oxford, 1982).
[16] G. Mathiak *et al.*, J. Non-Cryst. Solids **205-207**, 412 (1996).
[17] J. P. Foster and R. J. Reynik, Metall. Trans. A **4**, 207 (1973).
[18] V. I. Ogloblya, V. I. Lozovoi, and A. G. Chumakov, Phys. Metals **9**, 455 (1990).
[19] J. D. Verhoeven, Trans. Metall. Soc. AIME **242**, 1937 (1968).